Journal of Beijing Institute of Technology, 2021, Vol. 30, Suppl.1

Measurement Model and Dynamic Performance Analysis of Inlet Electrostatic Sensor on Aircraft Engine

Zhengxing Feng[1], Yu Fu[1,✉], Jinglin Wang[2], Yong Shen[2], Liang Cao[2] and Hongfu Zuo[3]

(1. Institute of Aviation Engineering, Civil Aviation University of China, Tianjin 300300, China; 2. Aviation Key Laboratory of Science and Technology on Fault Diagnosis and Health Management, Shanghai 201601, China; 3. College of Civil Aviation, Nanjing University of Aeronautics and Astronautics, Nanjing 211106, China)

Abstract: Online electrostatic monitoring technology, which is equipped with foreknowledge information for aircraft engine faults, can effectively enhance flight safety and reduce costs. This paper provides a theoretical foundation for inlet electrostatic sensor design, which is the key issue of this technology. First, the induced principle of inlet electrostatic sensor is analyzed. Then, factors affecting spatial sensitivity distribution are quantitatively analyzed to obtain the sensitivity distribution frequency spectrum and dynamic response performance. This sensor is equivalent to a low-pass spatial filter. Results show that bandwidth changes depending on particle speed, radial position, and axial length. The optimal ring size is designed accordingly, considering sensor sensitivity, uniformity, mechanical processing, and installation.

Key words: aircraft engine; air inlet; electrostatic sensor; sensitivity distribution; dynamic performance

CLC number: V231.25; TH89 **Document code:** A **Article ID:** 1004-0579(2021)S1-0202-08

Gas path electrostatic monitoring technology[1], which is an early fault monitoring method[2-4] for aircraft engines, could effectively get the realization of prognostics and health management (PHM)[5-7]. In this method, the inlet debris monitoring system (IDMS)[8] detects debris inhaled by the engine inlet and determines whether the debris caused damage to the engine gas path.

The electrostatic signal of the debris intake could be captured by the inlet electrostatic sensor in IDMS. The probe performance of this sensor is very important in ensuring the accuracy of signal parameters. Therefore, the simulation and optimization of the sensor probe model are necessary steps in obtaining the optimal model parameters of the electrostatic sensor. In addition, the frequency response characteristic of the electrostatic sensor is an important parameter that reflects the dynamic performance of the sensor. The filter effect of the sensor is analyzed according to the space distribution function. In this way, the frequency response characteristic of the sensor is obtained.

For the problems mentioned above, the sensitive field is analyzed in this paper through the ANSYS finite element analysis method based on the working principle and its sensing model for inlet electrostatic sensor. Moreover, the dynamic

Received 2020-06-11
Supported by Aeronautical Science Foundation of China (20183367013); the Fundamental Research Funds for the Central Universities of China (3122017027)
✉ Author for correspondence, Ph.D.
E-mail: fuyu00_@163.com
DOI: 10.15918/j.jbit1004-0579.20057

performances of the sensitivity structure and spatial sensing field are obtained, which provide the theoretical basis for the design of the sensor structure and signal processing circuit.

1 Probe Model of the Inlet Electrostatic Sensor

1.1 Model description

According to Gauss theorem, the electric flux for point charge is always proportional to the charge on its own. Thus, the influence of the electric field formed by the electric charge can be represented by an electric field that is excited by a point charge[9-10]. Assuming that there is a point charge q surrounded by a closed surface S, the electric flux from electric field E to the closed surface S can be expressed according to Coulomb's law as follows

$$\oint E\mathrm{d}S = \frac{q}{\varepsilon_0} \tag{1}$$

where q is the total charge within the closed surface, r is the radius of the spherical surface Gauss S, and E is the electric field generated on the surface Gauss S. According to Eq. (1), the flux on S can be derived as

$$\oint E\mathrm{d}S = 4\pi r^2 E = \frac{q}{\varepsilon} \tag{2}$$

where ε is the dielectric permittivity in vacuum, $\varepsilon=\varepsilon_0$, and medium, $\varepsilon=\varepsilon_r\varepsilon_0$; and ε_r is the relative permittivity. The electric field lines emitted by the point charge are incompletely converged on the probe surface because of the limited surface area of the probe. Thus, the point charge cannot be completely induced by the metal probe, that is, induced charge $q'<q$. In the model presented above, the closed surface flux along the metal probe surfaces delineated by a Gaussian closed surface can be approximately represented as

$$EA \sim \frac{q'}{\varepsilon} \tag{3}$$

where A is the probe surface, and q' represents the induced charge on the surface. The electric field intensity E is assumed to be approximately equal along the probe surface, and the combined Eqs. (2) (3) can be introduced as

$$q' \sim \frac{qA}{4\pi r^2} \tag{4}$$

where r is the distance from the point charge to the probe surface. Eq. (4) can be considered as an approximate response function of the electrostatic sensor. Therefore, in the ideal Gauss theorem model, as long as its surface characteristics are known, the sensitivity of the sensor is related to its charge quantity and space position.

Sensitivity is the main parameter of sensor performance, and it demands a symmetrical sensitivity to avoid the effect of airflow distribution. The sensor sensitivity in sensitive space could be defined as follows[11-12].

Sensor sensitivity in sensitive space is the absolute value of Q induced by point charge q. This sensor probe physical model indicates that the induced charge Q in sensitive space is only related to the point charge in radial position r and axial position x. Therefore, the finite element analysis model can be simplified into a two-dimensional (2D) model and the sensitivity of the sensor can be reduced to the following 2D form:

$$S(x,y) = \left|\frac{Q}{q(x,y)}\right| \tag{5}$$

$$Q = \int_l E\mathrm{d}l \tag{6}$$

where E is the curve flux and l is the electrostatic probe boundary. Therefore, the sensitivity distribution can be obtained by changing the radial and axial positions of the point charge.

A radial sensitivity variation parameter S_v is defined based on the concept of standard deviation and variation system as follows

$$S_{\mathrm{avg}} = \frac{1}{M}\sum_{i=1}^{M} S_{x,i} \tag{7}$$

$$S_{\mathrm{dev}} = \left(\frac{1}{M}\sum_{i=1}^{M}\left(S_{x,i} - S_{\mathrm{x,avg}}\right)^2\right)^{1/2} \tag{8}$$

$$S_v = \frac{S_{dev}}{S_{avg}} \tag{9}$$

where S_{avg} is the section average sensitivity, M (statistical population) is the sample number of section sensitivity, S_{dev} is the corresponding sensitivity deviation, and S_v is the sensitivity uniformity of a section. From Eq.(9), S_v is a function of the sensor structure parameters, in which the smaller the parameters S_v, the better the sensitivity distribution uniformity, indicating that the effect of the air flow pattern on the inlet charge value is smaller.

According to the probe structure and simulation requirements, this paper firstly simulates the physical area: electrode area, the area between the electrode and electrode shell insulation medium, and the air area of the space point charge. This model contains several parameters: insulating dielectric layer thickness H, relative dielectric permittivity ε, electrode axial length L, electrode thickness h, and ring electrode diameter D. The physical model of the sensor is shown in Fig. 1.

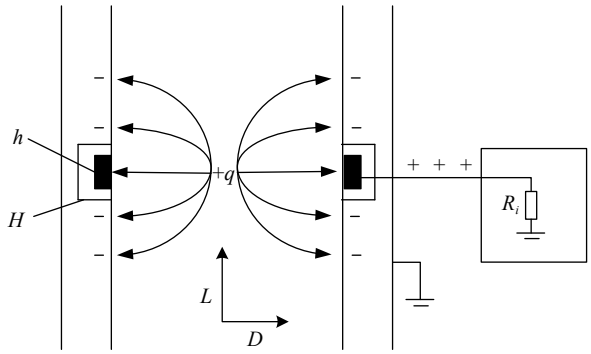

Fig. 1 Physical model of inlet electrostatic sensor

1.2 Model analysis

1.2.1 Insulation layer thickness to sensor sensitivity

The insulation layer thicknesses are 1, 2, 5, and 10 mm. The simulation results are calculated, as shown in Tab. 1.

Tab. 1 shows the average sensitivity S_{avg} and its variation parameters S_v with different thicknesses. When thickness H=1, 2, 5, 10 mm, the corresponding S_{avg} values are 0.5960, 0.5680, 0.5175, and 0.4685, respectively, whereas their changed parameters S_v are 2.76%, 2.53%, 2.20%, and 1.93%, respectively. These results suggest that S_v decreases gradually, and sensitivity tends to be uniformly distributed with the increase of insulation layer thickness.

Tab. 1 Average sensitivity and variation parameters of different insulation layer thicknesses

H/mm	S_{avg}	S_v/%
1	0.5960	2.76
2	0.5680	2.53
5	0.5175	2.20
10	0.4685	1.93

1.2.2 Dielectric permittivity of insulation layer to sensor sensitivity

Dielectric permittivities 1.00, 2.55, 3.75, and 5.00 are set to analyze the sensor sensitivity, as shown in Tab. 2.

Tab. 2 Average sensitivity and variation parameters of dielectric permittivity

ε	S_{avg}	S_v/%
1.00	0.4888	1.91
2.55	0.5680	2.53
3.75	0.5886	2.71
5.00	0.6003	2.81

Tab. 2 shows the S_{avg} values and their variation parameters S_v with different dielectric permittivities. When dielectric permittivity ε=1.00, 2.55, 3.75, 5.00, the corresponding S_{avg} values are 0.4888, 0.5680, 0.5886, and 0.6003, respectively, whereas their variation parameters S_v are 1.91%, 2.53%,2.71%, and 2.81%, respectively. These results suggest that S_v enlarges gradually with nonuniform sensitivity, along with the increase of the dielectric permittivities of the insulation layer.

1.2.3 Electrode axial length to sensor sensitivity

The axial lengths are set 4, 10, 20, and 40 mm. The simulation results are calculated and presented in Tab. 3.

Tab. 3 Average sensitivity and variation parameters of electrode axial length

L/mm	S_{avg}	S_v/%
4	0.4004	3.43
10	0.5680	2.53
20	0.7269	1.27
40	0.8971	0.18

Tab. 3 shows S_{avg} and its changed parameters S_v with different electrode axial lengths L. When L=4, 10, 20, 40 mm, the corresponding S_{avg} values are 0.4004, 0.5680, 0.7269, and 0.8971, respectively, while their variation parameters S_v are 3.43%, 2.53%, 1.27%, and 0.18%, respectively. These results indicate that S_v decreases gradually and sensitivity tends to be uniformly distributed with the increase of the electrode axial length.

1.2.4 Electrode thickness to sensor sensitivity

The electrode thicknesses are set to 0.5, 1.0, 2.0, and 5.0 mm. The simulation results are calculated, as shown in Tab. 4.

Tab. 4 Average sensitivity and variation parameters of electrode thickness

h/mm	S_{avg}	S_v/%
0.5	0.5463	2.98
1.0	0.5680	2.53
2.0	0.6023	2.00
5.0	0.6593	1.17

Tab. 4 shows S_{avg} and its changed parameters S_v with different electrode thicknesses. When electrode thickness h = 0.5, 1.0, 2.0, 5.0 mm, the corresponding S_{avg} values are 0.5463, 0.5680, 0.6023, and 0.6593, respectively, whereas the variation parameters S_v were 2.98%, 2.53%, 2.00%, and 1.17%, respectively, that is, S_v decreased gradually with uniform sensitivity with the increase of the electrode thickness.

1.2.5 Ring diameter to sensor sensitivity

The ring electrode diameters are set to 20, 50, 80, and 100 mm. The simulation results are calculated, as shown in Tab. 5.

Tab. 5 Average sensitivity and variation parameters of ring electrode diameter

D/mm	S_{avg}	S_v/%
20	0.6907	1.10
50	0.5680	2.53
80	0.5348	2.92
100	0.5199	3.14

Tab. 5 shows S_{avg} and its changed parameters S_v with different ring diameters D. When D=20, 50, 80, 100 mm, the corresponding S_{avg} values are 0.6907, 0.5680, 0.5348, and 0.5199, respectively, whereas their variation parameters S_v are 1.10%, 2.53%, 2.92%, and 3.14%, respectively, that is, S_v increases gradually and sensitivity tends to be uniformly distributed with the increase of the ring diameter.

2 Dynamic Performance Analysis of Inlet Electrostatic Sensor

The probe axial length is w. According to the probe symmetry structure, the charged particles pass along the central axis of the ring electrode, and the spatial position of sensitivity can be expressed by axial x and radial r.

The analysis of the dynamic characteristics of the electrostatic sensor probe is based on the spatial sensitivity distribution function. Fig. 2 shows the sensitivities along axial x and radial r. As can be seen, the sensor sensitivity increases to a peak at a certain radial position r and then decreases when the point charge moves along axial direction. In addition, on the ring center section x=0, sensor sensitivity is higher closer to the ring. Third, sensitivity changes sharply close to the ring with faster sensitivity decrease. Therefore, the sensitive space of the sensor is different when particles move along the axial direction at different radial positions r, and such sensitive space at the center of the cross section is larger. Sensitivity decreased to a certain threshold because the sensitivity of the different radial positions along the axial direction also decreased.

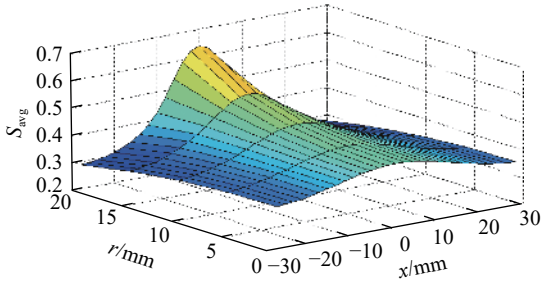

Fig. 2 Sensitivity in space position

Fig.2 shows that the sensor sensitivity is consistent with the trend of the bilateral exponential and Gauss pulse functions. Therefore, the sensitivity distribution of the sensor is based on the double exponential and Gauss pulse functions.

Bilateral exponential function $f_3(x) = ae^{-b|x|}$

Gauss pulse function $f_1(x) = ae^{-\left(\frac{x-b}{c}\right)^2}$

The sensitivity distribution data of 29 axial positions were obtained by ANSYS simulation, and the data were fitted by using the abovementioned function. The fitting results are shown as follows: root mean square error (RMSE), correlation coefficient square (R-Square), and residual sum of squares (SSE). Specifically, the smaller the SSE and RMSE, the bigger the R-Square, indicating that the fitting effect is better. The fitting effect and evaluation index are shown in Fig. 3 and Tab. 6, respectively. Therefore, the fitting effect of the two basic Gauss functions is optimal.

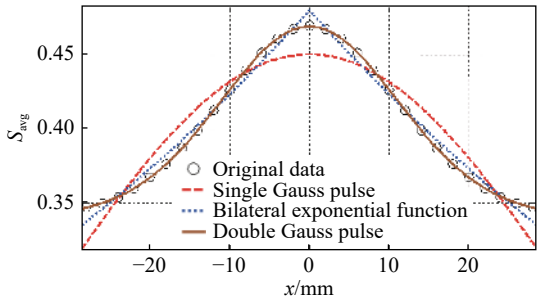

Fig. 3 Fitting effect of different functions

Tab. 6 Evaluation indexes of different fitting functions

r/mm	Single Gauss pulse function			Double Gauss pulse function			Bilateral exponential function		
	RMSE	R-Square	SSE	RMSE	R-Square	SSE	RMSE	R-Square	SSE
0	0.00357	0.9184	0.0003314	0.00068	0.9971	1.168×10^{-5}	0.00142	0.9865	5.464×10^{-5}
5.0	0.00886	0.9228	0.0020400	0.00115	0.9987	3.320×10^{-5}	0.00363	0.9866	0.0003549
7.5	0.01082	0.9161	0.0030440	0.00025	1.0000	1.556×10^{-6}	0.00420	0.9869	0.0004755
10.0	0.01417	0.9013	0.0052240	0.00030	1.0000	2.220×10^{-6}	0.00540	0.9851	0.0007892
12.5	0.01918	0.8859	0.0095690	0.00052	0.9999	6.747×10^{-6}	0.00724	0.9831	0.001416
15.0	0.02706	0.8600	0.0190300	0.00086	0.9999	1.847×10^{-5}	0.01077	0.9770	0.00313
17.5	0.03950	0.8260	0.0405600	0.00139	0.9998	4.815×10^{-5}	0.01696	0.9667	0.007765
20.0	0.05888	0.7811	0.0901200	0.00236	0.9997	0.0001394	0.02778	0.9494	0.02084

3 Results and Discussion

3.1 Spatial filtering effect

The electrostatic field is distributed in the sensing space, which is closely related to the geometric structure of the ring. The electrostatic information is not completely transformed by the sensor signal output and weighted average with specific weight function $s(x, r)$. This information modulation effect is called the spatial filtering effect[13].

The induced charge is expressed as

$$Q = \iint q(x,r)\cdot s(x,\ r)\mathrm{d}x\mathrm{d}r \qquad (10)$$

where $q(x,\ r)$ is the distribution of charged particles in the sensor space. Assuming that the charged particles moving along the axial direction at velocity v, Eq. (10) is expressed as

$$Q(t) = \iint q(x+vt,r)\cdot s(x,r)\mathrm{d}x\mathrm{d}r \qquad (11)$$

Therefore, the velocity of the charged particles can induce the change of the induced field and charge. Induction charge function is only related to the direction of the axial x, so it can be simplified as weighting function $s(x)$. Meanwhile, $s(x)$ is a sensitivity function expressed as[14]:

$$S(w_x)=\int\left[a\mathrm{e}^{-(bx)^2}+c\mathrm{e}^{-(dx)^2}\right]\mathrm{e}^{-\mathrm{j}w_x}\mathrm{d}x=\frac{a\sqrt{\pi}}{b}\mathrm{e}^{-\left(\frac{w_x^2}{4b^2}\right)}+\frac{c\sqrt{\pi}}{d}\mathrm{e}^{-\left(\frac{w_x^2}{4d^2}\right)} \quad (12)$$

In the same radial position, the axial sensitivity distribution function $s(x)$ is changed into $s(w_x)$ by using the spatial domain Fourier transform, where $s(w_x)$ is the transfer function of the axial sensitivity space, w_x is the sensor angular frequency, and the corresponding spatial frequency f_x transfer function is expressed as

$$S(f_x)=\frac{a\sqrt{\pi}}{b}\mathrm{e}^{-\left(\frac{\pi^2 f_x^2}{b^2}\right)}+\frac{c\sqrt{\pi}}{d}\mathrm{e}^{-\left(\frac{\pi^2 f_x^2}{d^2}\right)} \quad (13)$$

The spatial spectrum distribution of the electrostatic sensor in different radial positions r is shown in Fig. 4. The graph shows that a low frequency signal passes through in the space frequency domain while a high frequency signal is cut off. Therefore, the front end of the electrostatic sensor is equivalent to the spatial low pass filter. In addition, the spatial filtering characteristics of the sensor on different radial positions r are not consistent, that is, the larger the r is, the wider the spatial spectrum.

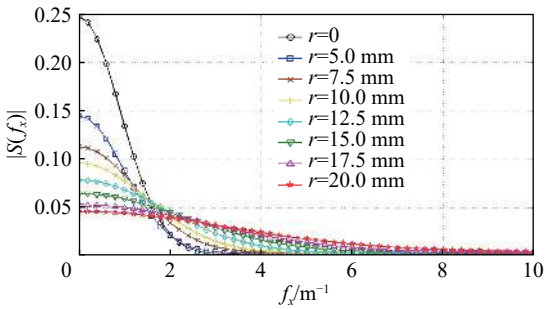

Fig. 4 Spatial spectrum distribution with different radial positions

Fig. 5 shows the spatial filtering characteristics when the axial lengths of w are 10 and 20 mm. The axial working frequency bandwidth is known to have little difference when it is in the same radial position. However, when the axial position takes a certain value with the increase of the radial distance, the response frequency band becomes wider, and the response ability of the sensor to high frequency signal is obviously enhanced. At the working band and radial position r=0 mm, the sensor response ability increases with the axial length, whereas the response ability changes slightly at radial position r=15 mm.

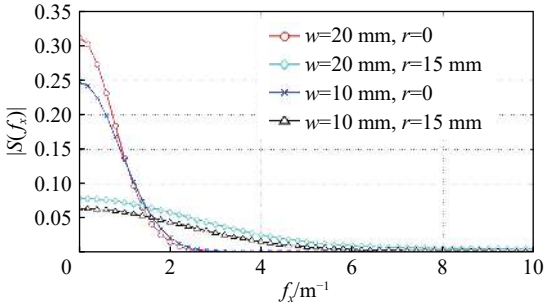

Fig. 5 Spatial spectrum distribution with different axial lengths

3.2 Frequency response characteristic analysis

3.2.1 Frequency response characteristic

In the same radial position, the input signal of the point charge can be expressed as impulse signal $\delta(x+vt)$; hence, the output unit impulse response function $h(t)$ is given as

$$h(t)=\int\delta(x+vt)S(x)\mathrm{d}t \quad (14)$$

According to the impulse function property given by

$$\int f(t)\delta(t-t_1)\mathrm{d}t=f(t_1),\ h(t)=S(-vt) \quad (15)$$

the frequency response of the sensor can be shown as

$$H(f)=\int h(t)\mathrm{e}^{-(\mathrm{j}2\pi f(t))}\mathrm{d}t=\frac{1}{v}S\left(-\frac{f}{v}\right)=\frac{a}{bv}\sqrt{\pi}\mathrm{e}^{-\left(\frac{\pi^2 f^2}{b^2 v^2}\right)}+\frac{c}{dv}\sqrt{\pi}\mathrm{e}^{-\left(\frac{\pi^2 f^2}{d^2 v^2}\right)} \quad (16)$$

3.2.2 Factor analysis of the frequency characteristics

Assuming the point charge passes through the probe sensitivity space at a velocity of 5 m/s, the sensor frequency response is analyzed according to Eq. (16). Fig. 6 shows that the sensor is a low pass filter in the time domain. At a certain axial position, the response frequency band widens with the increase of the radial distance.

Eq. (16) shows that the frequency characteristics of the induced charge are related to the

moving speed of the charged particles. Fig. 7 shows that the charged particles pass faster and the frequency response of the induced charge becomes wider when the charge passes through the ring at rates of 5 and 10 m/s in the same radial position.

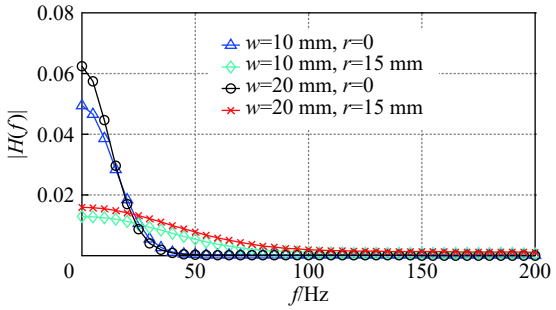

Fig. 6 Frequency response characteristics with different axial lengths

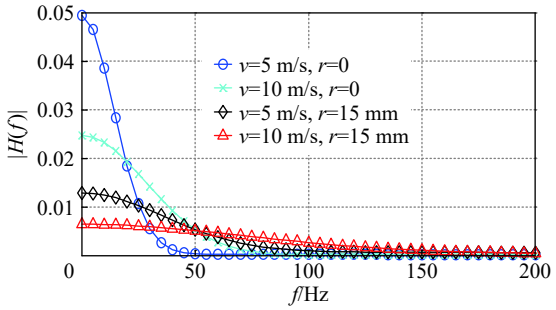

Fig. 7 Frequency response characteristics with different particle velocities

4 Conclusions

In this paper, the factors affecting the inlet sensor spatial sensitivity distribution and its dynamic performances are quantitatively analyzed with the electrostatic sensor sensitivity mathematical model and inlet structural features. First, the sensitivity and its uniformity should be considered for the sensor physical design structure. Second, the sensor sensitivity, sensitivity uniformity, machining, installation, and other factors should be considered comprehensively for the ring probe design size, which should have the following properties: thickness of insulating layer H=2 mm, insulating layer dielectric permittivity ε=2.55, axial length of ring electrode L=10 mm, ring electrode thickness h=1 mm, and diameter D=50 mm. These findings can provide manufacturers with insights regarding the physical structure of band width. Third, the sensitivity distribution function is obtained by using the sensitivity data of the different axial positions. The results show that the fitting degree of two Gauss pulse functions is optimal. The independent variable of the sensitivity distribution function is the axial distance, and its coefficient depends on the radial distance. Finally, the spatial filtering effect and frequency response characteristics show that low frequency signal passes through and high frequency signal is cut-off in the space and time domains; in this case, the larger the radial distance r, the wider that spatial frequency spectrum and frequency response range. On the same radial position, the time domain frequency response becomes greater with the increase of the axial length; in this case, particles pass through the ring faster and the frequency response band of the induced charge becomes wider. Therefore, the frequency response and sensing space of the electrostatic sensor can be enlarged by properly increasing the ring axial length.

References:

[1] Wen Zhenhua, Hou Junxing, Atkin Jason. A review of electrostatic monitoring technology: The state of the art and future research directions [J]. Progress in Aerospace Sciences, 2017, 94: 1-11.

[2] Wen Zhenhua, Hou Junxing, Jiang Zhiqiang. Formation mechanism analysis and detection of charged particles in an aero-engine gas path [J]. International Journal of Aeronautical and Space Sciences, 2015, 16(2): 247-253.

[3] Fu Yu, Yin Yibing, Feng Zhengxing, et al. A method for engine performance evaluation by fusing electrostatic signal and gas path parameters [J]. Journal of Propulsion Technology, 2019, 40(2): 449-455.

[4] Fu Yu, Wei Dongdong, Zuo Hongfu, et al. Time sequence change-point model of electrostatic state parameters of aircraft engine [J]. Transactions of Nanjing University of Aeronautics & Astronautics, 2018, 35(1): 126-134.

[5] Fisher C. Data and information fusion for gas path

debris monitoring[C]// IEEE Proceedings of Aerospace Conference, 2001, 6: 3017-3022.

[6] Novis A, Powrie H. PHM sensor implementation in the real world: A status report[C]// IEEE Proceedings of Aerospace Conference, 2006: 1-9.

[7] Melissa Wilcox, David Ransom, Meron Henry, et al. Engine distress detection in gas turbines with electrostatic sensors[C]// Proceedings of ASME Turbo Expo 2010: Power for Land, Sea and Air, 2010.

[8] Fu Yu, Yin Yibing, Zuo Hongfu. Aero-engine exhaust electrostatic monitoring and signal characteristics analysis [J]. Chinese Journal of Scientific Instrument, 2018, 39(2): 160-168.

[9] Yan Y, Byrne B, Woodhead S, et al. Velocity measurement of pneumatically conveyed solids using electrodynamic sensors [J]. Measurement Science and Technology, 1995, 6: 515-537.

[10] Rahmat M F, Thuku I T, Tajdari T, et al. Sensing and filtering characteristics of electrostatic sensors for pneumatically conveyed particles [J]. International Journal of Physical Sciences, 2011, 6(22): 5091-5103.

[11] Wen Z, Ma X, Zuo H. Characteristics analysis and experiment verification of electrostatic sensor for aero-engine exhaust gas monitoring [J]. Measurement, 2014, 47(1): 633-644.

[12] Xu Y, Zuo H, Zhan Z, et al. Optimal design of electrostatic sensor based on sensitivity analysis [J]. Chinese Journal of Scientific Instrument, 2012, 33(5): 1084-1089.

[13] Wu Xinjie, Zhang Jiancheng. Applications of morphological filter and spatial filter to velocity measurement of two-phase flow [J]. Chinese Journal of Sensors & Actuators, 2007, 20(9): 2124-2127.

[14] Xu C. Finite element analysis of the sensing field of electrodynamic sensor [J]. Chinese Journal of Scientific Instrument, 2007, 28(7): 1311-1318.